

RESEARCH ARTICLE | APRIL 24 2023

A high-precision silicon-on-insulator position sensor

Paul Beck ; Laura C. Wynne; Simone Iadanza; ... et. al

APL Photonics 8, 046113 (2023)

<https://doi.org/10.1063/5.0133968>View
OnlineExport
Citation

CrossMark

Articles You May Be Interested In

Calculations of free energy of surface interactions in crystalline polyethylene

J. Chem. Phys. (July 2018)Water adsorption induced in-plane domain switching on BaTiO₃ surface*Journal of Applied Physics* (September 2015)**APL Photonics**Special Topic: State-of-the-art and Future
Directions in Optical Frequency Combs**Submit Today!**

A high-precision silicon-on-insulator position sensor

Cite as: APL Photon. 8, 046113 (2023); doi: 10.1063/5.0133968

Submitted: 7 November 2022 • Accepted: 5 April 2023 •

Published Online: 24 April 2023



View Online



Export Citation



CrossMark

Paul Beck,^{1,2,a)}  Laura C. Wynne,³ Simone Iadanza,^{4,5}  Liam O'Faolain,^{4,5}  Sebastian A. Schulz,³ 
and Peter Banzer^{1,2,6} 

AFFILIATIONS

¹Max Planck Institute for the Science of Light, Staudtstr. 2, D-91058 Erlangen, Germany

²Department of Physics, Institute of Optics, Information and Photonics, Friedrich-Alexander-University Erlangen-Nuremberg, Staudtstr. 7/B2, D-91058 Erlangen, Germany

³School of Physics and Astronomy, SUPA, University of St Andrews, North Haugh, St Andrews KY16 9SS, United Kingdom

⁴Centre for Advanced Photonics and Process Analysis, Munster Technological University, Bishopstown, T12 P928 Cork, Ireland

⁵Tyndall National Institute, Lee Maltings, Dyke Parade, T12 R5CP Cork, Ireland

⁶Institute of Physics, NAWI Graz, University of Graz, Universitätsplatz 5, Graz 8010, Austria

^{a)} Author to whom correspondence should be addressed: paul.beck@mpl.mpg.de

ABSTRACT

Integrated photonic devices provide significant advantages over their conventional counterparts, such as a drastically reduced footprint as well as compatibility with other photonic or electronic circuitry. In this work, we present a high-precision optical position sensor fabricated on a silicon-on-insulator platform. The sensor relies on the principle of position-dependent directional waveguide coupling upon excitation of a monolithically integrated scatterer with a tightly focused polarization-tailored beam. We demonstrate a spatial resolution of 7.2 nm, corresponding to approximately $\lambda/200$.

© 2023 Author(s). All article content, except where otherwise noted, is licensed under a Creative Commons Attribution (CC BY) license (<http://creativecommons.org/licenses/by/4.0/>). <https://doi.org/10.1063/5.0133968>

I. INTRODUCTION

Over the last two decades, the field of silicon photonics has experienced enormous growth. This development is mainly caused by the ever-increasing demand for higher data transmission rates in telecommunication, the miniaturization of optical devices, various applications in sensing, and many more. One key factor enabling the large-scale production and implementation of silicon photonic devices is their compatibility with well-established integrated circuits technology, which is based on similar fabrication techniques.^{1–3} Basic integrated structures in a silicon-on-insulator (SOI) platform, such as nanophotonic waveguides, grating couplers, and spot size converters, have been demonstrated already back in 2004,⁴ paving the way for more sophisticated and powerful devices like on-chip sensors,⁵ meshes of Mach-Zehnder interferometer and phase shifters,⁶ or integrated spectrometers.⁷

However, the development of on-chip integrated devices enabling alignment and displacement measurements is still in its infancy. Therefore, the industrial standard mostly relies on off-chip sensors and image processing, contributing to the large device cost. Hence, high resolution displacement sensing is not achievable in many applications where it would be desired, for example, hybrid integration or packaging of nanophotonic devices. Even high-end lithography systems often feature alignment accuracy on the order of several 100 nm.⁸ Nanometer resolution has, however, been reached in the localization of individual nano- or micrometer-sized particles, employing a large variety of established techniques. These range from fluorescence microscopy^{9,10} to the camera-based interferometric detection of light scattered by a particle, utilizing its diffraction-limited image.¹¹ Recently, a method based on the directional scattering by an individual silicon nanoparticle, excited with a tightly focused polarization-tailored beam, has been demonstrated,

resulting in sub-nanometer and sub-angstrom resolution.^{12,13} Moreover, some of the authors of this article have previously also presented a first step toward an all-integrated implementation of this approach.¹⁴ However, this demonstration required a rather demanding fabrication step, i.e., the placement of a single spherical nanoparticle on a pre-fabricated photonic crystal waveguide architecture by pick-and-place handling in a scanning electron microscope. This demonstration served the purpose of a proof-of-concept when it comes to integration. Nonetheless, it is not scalable, requires the utilization of special equipment going beyond standard fabrication facilities, and the mechanical stability might also be limited. Here, we now introduce and study, both numerically and experimentally, an SOI based position sensor that features full monolithic integration of the scatterer, realized via an in-plane silicon cylinder surrounded by silicon waveguides. This device represents a low-cost, high-accuracy alternative to the aforementioned standard methods. The optical output of the device is directly linked to both the direction and magnitude of its displacement, making it particularly suitable for highly precise alignment in nanolithography systems.

II. THEORETICAL CONSIDERATIONS AND SAMPLE DESIGN

Tightly focused, polarization-structured light fields constitute a versatile tool for the tailored excitation of nano- and microscopic structures.^{15,16} This owes mainly to their sculpted and complex electromagnetic fields and phase distributions. Especially for the purpose of nano-localization, vector beams exhibiting a cylindrical symmetric distribution are a suitable choice. Upon tight focusing, an azimuthally polarized doughnut beam is converted into a strongly confined electromagnetic landscape featuring position-dependent three-dimensional fields with interesting and favorable features, especially in a sub-wavelength region close to the optical axis. Here, the electric and magnetic fields depend approximately linearly on the transverse coordinates x and y ,

$$\mathbf{E}(x, y) \propto -yE_t^0 \mathbf{e}_x + xE_t^0 \mathbf{e}_y, \quad (1)$$

$$\mathbf{H}(x, y) \propto xH_t^0 \mathbf{e}_x + yH_t^0 \mathbf{e}_y + iH_z^0 \mathbf{e}_z. \quad (2)$$

The relevant, i.e., nonzero components, of the electromagnetic fields of a tightly focused azimuthally polarized beam are shown in Fig. 1(a). Due to the fields' inherent symmetry, we choose a depiction in cylindrical coordinates. Here, only the azimuthal electric (E_ϕ) as well as the radial and longitudinal magnetic (H_r , H_z) field components are nonzero. As will become clear in the following, the features that make such a beam especially well-suited for our application are (1) the cylindrical symmetry and (2) the emergence of a strong longitudinal magnetic field component. As shown in the [supplementary material](#), both of these features are not present in a conventionally linearly polarized Gaussian beam. As mentioned earlier, in our scheme, an in-plane silicon cylinder will serve as the coupler between the incoming light and the silicon waveguide architecture. Its scattering characteristics can be described by a wavelength-dependent superposition of electric and magnetic multipoles of different

amplitudes and phases. The strength of the individual contributions is determined by the light fields used for excitation, the geometry of the silicon cylinder, and its refractive index relative to the surrounding medium. The scattering process can be described by the scattering matrix (T-matrix) formalism. Here, both the incoming and scattered fields are expressed in terms of vector spherical harmonics (VSHs) describing multipole fields with respective amplitude coefficients $a_{mn}^{in(sc)}$, $b_{mn}^{in(sc)}$, which can be summarized in vectors $\mathbf{A}^{in(sc)}$, $\mathbf{B}^{in(sc)}$. The superscripts *in* and *sc* denote incoming and scattered fields, respectively. The T-matrix relates these amplitude coefficients via $[\mathbf{A}^{sc}, \mathbf{B}^{sc}] = \hat{\mathbf{T}} [\mathbf{A}^{in}, \mathbf{B}^{in}]$. The advantage of this method is that the T-matrix depends solely on the geometry and refractive index of the scatterer (and its surroundings) and not on the excitation fields. For a spherical scatterer, the elements of the T-matrix, which determine the relative strength of the supported electric and magnetic multipoles, depend on the radius of the sphere, its relative refractive index with respect to the surrounding medium, and the wavelength of the light. For a non-spherical scatterer, the computation of the T-matrix is more demanding. Schematically speaking, the expansion of the in- and outgoing fields in spherically symmetric functions fails for this symmetry. However, by using a set of distributed,

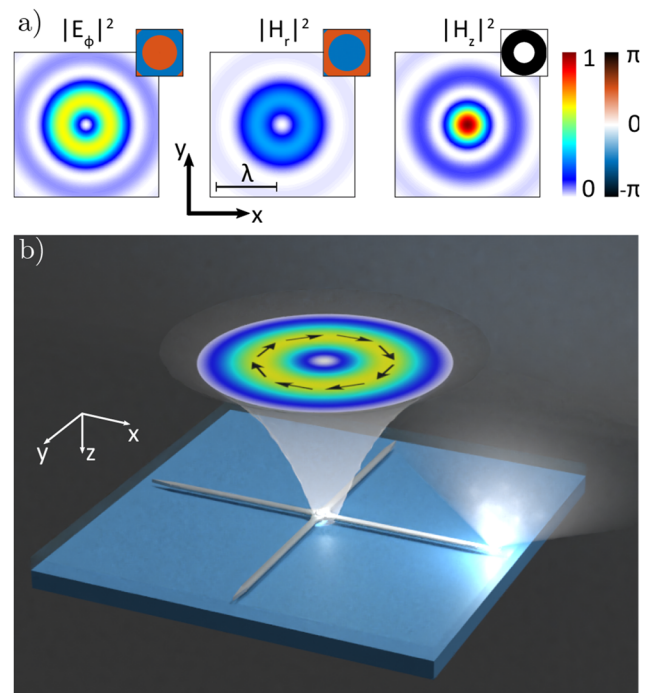


FIG. 1. Excitation fields and the working principle of the position sensor. (a) Electromagnetic fields of a tightly focused azimuthally polarized beam, which is used for excitation of the integrated scatterer. The spatial extent of the field distributions relative to the wavelength is shown by the inserted scale bar. The insets show the relative phases of the respective field components. (b) Schematic of the SOI-based device. Excitation of the central cylinder leads to position-dependent directional coupling of scattered light into the four waveguides surrounding it. The waveguides are terminated by a narrow taper, followed by a scattering edge (not shown here), which couples light out of the plane while minimizing back-reflections.

discrete sources, the applicability of the previously described method can be extended to particles of arbitrary shape, which has been introduced as the “null-field method with discrete sources.”^{17,18} Using this method, we design the silicon cylinder such that it predominantly supports electric and magnetic dipole and quadrupole moments at the telecommunication wavelength of 1550 nm. This is a prerequisite for directional coupling to occur upon illumination with the above-described tightly focused azimuthally polarized beam. The phenomenon of directional emission in the transverse plane by a di- or multipolar scatterer is known as transverse Kerker scattering. It was shown that this effect can be utilized for the localization of a single nanoparticle with sub-angstrom precision.^{12–14,19} With the emission of the excited multipoles interfering with each other directionally in dependence on their respective symmetries and strengths, also the in-coupled light will be asymmetrically distributed across the four waveguides. For simplification, we assume that the cylinder is homogeneously embedded in glass with a refractive index of 1.5 and do not take into account the surrounding waveguides. This is sufficient to obtain a good estimate of the spectral position of the multipole resonances. To implement the cylinder on an SOI platform, its height is limited to 220 nm, the thickness of the silicon layer. The optimal radius found by employing the modified T-matrix formalism mentioned above is 250 nm. Deviations of the cylinder geometry from this radius would lead to a shift in their spectral dependence, causing varying amplitude ratios of the respective excited di- and multipole moments. As transverse Kerker scattering relies on the interference of magnetic and electric dipole moments of similar strength, this would eventually lower the scattering directionality. However, since the dipole resonances exhibit a rather broad spectral dependence, there is considerable tolerance regarding the size of the scatterer within which one still observes directional emission. A detailed discussion of the multipole decomposition for the total scattering cross section can be found in the [supplementary material](#).

As shown schematically in [Fig. 1\(b\)](#), the cylinder is surrounded by four waveguides. Upon illumination of the cylinder with a tightly focused beam of light, different combinations of electric and magnetic multipoles are excited, with their relative amplitude and phase depending on the location of the cylinder with respect to the impinging focal field distribution. The scattered light is then coupled into the waveguides. The structured excitation consequently leads to position-dependent coupling due to transverse Kerker scattering, which is the core of the working principle of our device. In order to create a homogeneous and symmetric environment for the scattering cylinder and the waveguides, the entire light-processing silicon layer is embedded in a glass substrate and cladding. To optimize the geometry of the central scatterer and the surrounding waveguides, numerous effects need to be considered. First, the proximity of the waveguides to the cylinder affects both the resonant behavior of the latter as well as the near fields surrounding it. This is revealed by a numerical analysis of the system. It is important to note that impedance and polarization matching between the near fields and the propagating modes supported by the waveguides also play a crucial role. Furthermore, the spatial overlap of the focal field distribution with the ends of the waveguides changes depending on the relative position of the beam and sample, which again impacts the coupling behavior. All these dependencies need to be taken into account in the final design of the structure. After

performing a numerical optimization, we choose waveguides conforming to the silicon photonics standard, i.e., having a height of 220 nm and a width of 490 nm. The distance between the ends of the waveguides and the boundaries of the cylinder is limited to ~ 100 nm, ensuring an efficient coupling. To further optimize the coupling, the waveguide width is adiabatically decreased from 550 to 490 nm with increasing distance to the cylinder. After a total length of $43 \mu\text{m}$, the waveguides are terminated using inverse tapers, resulting in four output ports that emit light with a power corresponding to the power contained in the respective waveguide mode. The inverse tapers are employed and designed in a way that minimizes back-reflections and maximizes the out-coupling efficiency. Therefore, directional coupling to the waveguides, induced by a displacement of the sample, leads to a stronger emission from one of the output ports compared to the other three, as depicted in [Fig. 1\(b\)](#). Consequently, the position of the sample is encoded in the asymmetry of the light detected at the four respective output ports.

III. SAMPLE FABRICATION

The sample is fabricated using standard SOI processing techniques. The pattern is defined in ZE520A resist using a Raith Eline 30 kV electron-beam lithography system. The pattern is then transferred into the silicon layer using reactive ion etching with a CHF₃/SF₆ gas mixture (equal flow rate, 100 sccm). The central part as well as one of the out-couplers of the resulting structure can be seen in [Fig. 2](#). All elements of the device (the cylindrical scatterer, waveguides, and tapered out-coupler) are defined using a single electron-beam exposure and etch step, ensuring perfect alignment between them and removing uncertainty associated with the pick-and-place approach of previous implementations.¹⁴ The top cladding consists of three spin-coated layers of Accuglass 512Ba, with intermediate baking at 180 °C followed by a final 425 °C hard bake, resulting in a $\sim 2 \mu\text{m}$ thick top cladding.

IV. EXPERIMENTAL METHODS

In order to simultaneously access the in- and out-coupling ports of the fabricated device, we place it in a customized nano-optics setup,¹⁴ which is depicted in [Fig. 3\(a\)](#). This arrangement enables both the coupling of light to the structure via the illumination of the central scatterer and the measurement of the intensity emitted by the four out-couplers by imaging the whole device.

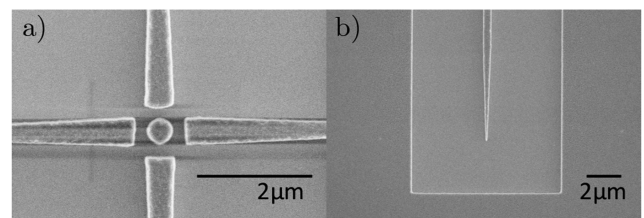


FIG. 2. Scanning electron micrographs of the device, showing (a) the central cylindrical scatterer and coupling region and (b) one of the tapers for out-coupling. The micrograph was taken before the deposition of the top cladding layer.

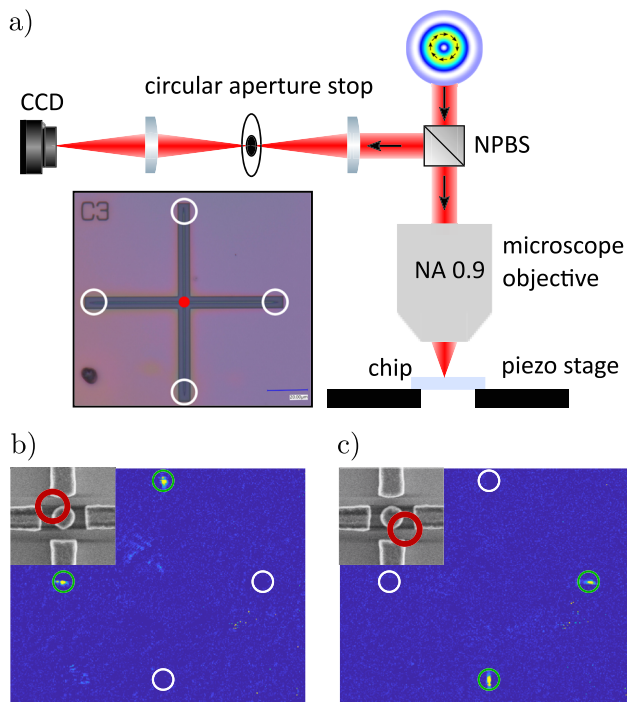


FIG. 3. (a) Sketch of the experimental setup. An azimuthally polarized beam of light is tightly focused on the sample using a high numerical aperture (NA) microscope objective. The sample is placed on a high-precision piezo stage and imaged onto a CCD camera using the same microscope objective and two additional lenses. We place a circular aperture stop in the image plane of the first lens to block the light directly reflected from the sample. This image is then projected onto the CCD camera. The inset shows a microscope image of the structure, where the positions of the out-couplers and the focal spot are indicated by white circles and a red dot, respectively. (b) and (c) Background-corrected camera images for two different positions of the structure with respect to the beam (see inset), separated by a shift of 160 nm in the x and y directions. Green and white circles indicate the out-couplers with nonzero and close-to-zero signals, respectively.

An azimuthally polarized beam of light at a wavelength of $\lambda = 1550$ nm is tightly focused onto the central area of the sample using a microscope objective (MO) with a numerical aperture of $NA = 0.9$, leading to tailored excitation of the scatterer and coupling into the waveguides. In order to position the sample with respect to the excitation fields, it is mounted on a high-precision 3D piezo stage. To measure the intensity of the light emitted at each of the four out-couplers, we image the structure in reflection. The imaging setup comprises the same MO that is focusing the beam earlier in its path, a non-polarizing beam splitter (NPBS), two lenses, and a CCD camera. The first lens creates an intermediate image of the sample, where we place a circular aperture stop in order to block the bright central spot resulting from the reflection of the focused beam by the sample. The plane of the aperture stop is then imaged again onto the CCD camera. The inset of Fig. 3(a) shows an image of the sample with the position of the focal spot indicated by a red dot. The four out-couplers are highlighted by white circles. Figs. 3(b) and 3(c) show exemplary background-corrected camera images for two different positions of the sample, as indicated by the respective

insets. In both images, the positions of the out-couplers with the nonzero and close-to-zero signals are indicated by green and white circles, respectively. The major difference between the two snapshots is indeed caused by a sample displacement of 160 nm in the x and y directions. For position 1 [Fig. 3(b)], light is predominantly coupled into the left-hand and upper waveguides and emitted from the respective waveguide ends, while there is no signal from the other two out-couplers. The situation is reversed for position 2 [Fig. 3(c)], resulting from a displacement in the opposite direction. These images show that (1) it is possible to couple light into the chip via illumination of the central scatterer and (2) the coupling to the waveguides is indeed strongly directional, depending on the position of the structure relative to the beam.

To quantitatively determine the directionality of the coupling, we first obtain the emitted intensity by integrating over the four respective areas of the camera image corresponding to the location of the out-couplers. We denote the resulting values as $I_{\pm x}$ and $I_{\pm y}$, where the coordinates x and y refer to the local coordinate system of the sample. Then, we compute the so-called directivities, which are the relative intensity differences in the x and y directions, respectively,

$$D_x = \frac{I_{+x} - I_{-x}}{I_{+x} + I_{-x}}, \quad (3)$$

$$D_y = \frac{I_{+y} - I_{-y}}{I_{+y} + I_{-y}}. \quad (4)$$

The directivity, together with a suitable calibration technique, can be employed to assess the sensitivity and accuracy of the position sensor.

V. RESULTS

To determine how sensitively the coupling directionality responds to a displacement of the sample and to calibrate the sensor for further measurements, we move the entire structure, consisting of the single cylindrical scatterer and the four waveguides surrounding it, across an area of $1 \times 1 \mu\text{m}^2$ in steps of 100 nm, which is centered with the focal field distribution. At each individual position of the scan, we take a camera image and calculate the corresponding directivities as defined in Eqs. (3) and (4). The resulting directivity maps are shown in Fig. 4, where we also compare them to numerical results. The latter ones were obtained from finite-difference time-domain (FDTD) simulations of the system. First of all, the experimentally obtained data qualitatively agree well with the simulation results regarding the sign and overall shape of the $x - y$ directivity maps. The quantitative difference between simulation and experiment of about one order of magnitude can be mostly attributed to imperfections resulting from the fabrication. This includes, e.g., deviations of the scatterer and waveguide geometry from the ideal shape assumed in the simulations. Moreover, the surface roughness of both the silicon and the surrounding glass might lead to propagation losses in the waveguides. For both datasets, we observe a zero crossing of both D_x and D_y close to their respective origins ($x = 0$ and $y = 0$). We further note that the sign of the directivity is opposite to the sample displacement, i.e., a displacement in the positive x (y) direction from the center leads to a negative D_x (D_y), and

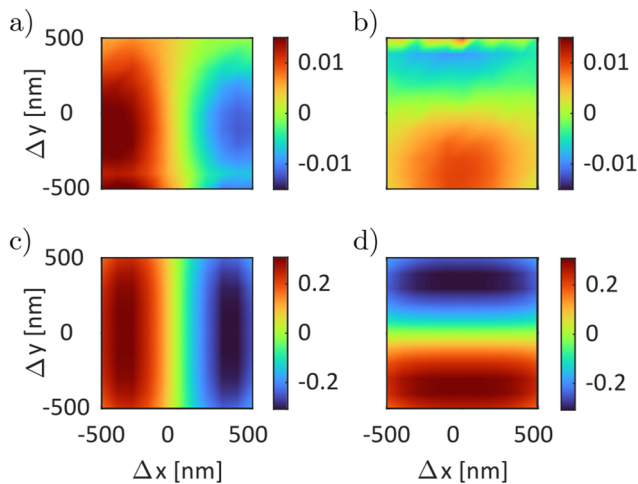


FIG. 4. Calculated directivities for a scan area of $1 \times 1 \mu\text{m}^2$. We show the experimentally obtained D_x (a) and D_y (b) and compare them to their numerically computed counterparts (c) and (d). The step size for the scans is 100 nm. The data have been interpolated in order to facilitate the comparison of numerical and experimental data.

vice versa. This result is a combination of the multipolar behavior of the cylinder and the surrounding waveguides, as well as the overlap of the fields scattered by the cylindrical scatterer with the TE (TM) waveguide mode. Furthermore, the impedance matching between the near fields surrounding the cylinder and the respective waveguide modes strongly influences the resulting directionality of the coupling. In the central region of the scans, i.e., for $r \ll \lambda$, we observe a linear dependence $D_x(x)$ ($D_y(y)$) with very little cross-dependence $D_x(y)$ ($D_y(x)$). This results from the linear behavior of the electromagnetic focal fields in this region. This linear relationship flattens out at larger distances from the center following the focal field distribution.

To calibrate the displacement sensor, we fit a plane described by an equation of the form $(D_x, D_y) = \hat{\mathbf{M}} \cdot (x, y)$ over an area of $200 \times 200 \text{ nm}^2$ around the center, even accounting for the slight cross-dependence. Inversion of this equation leads to the relations $x(D_x, D_y)$ and $y(D_x, D_y)$, enabling reconstruction of the particle position from the measured directivity. An example of such a calibration map is shown in Fig. 5, where we plot the experimentally measured D_x together with the fitted plane. To account for tiny changes in the focal fields that might occur due to drifts in the setup, a calibration is recorded prior to every measurement.

From the calibration measurement, it is also possible to determine the sensitivity of the sensor, i.e., the change in directivity for a certain displacement. From the data shown in Fig. 5, we obtain a directivity change of $\Delta D_x = 6.3 \cdot 10^{-5}/\text{nm}$ for D_x and $\Delta D_y = 2.9 \cdot 10^{-5}/\text{nm}$ for D_y . The difference in sensitivity in the x and y directions results most likely from a slight asymmetry of the scatterer and the surrounding waveguides.

In order to obtain an estimate of the accuracy and precision of the sensor, we perform a line scan along the x axis, where we move the sample in an interval of $-100 \text{ nm} \leq \Delta x \leq 100 \text{ nm}$ relative to the

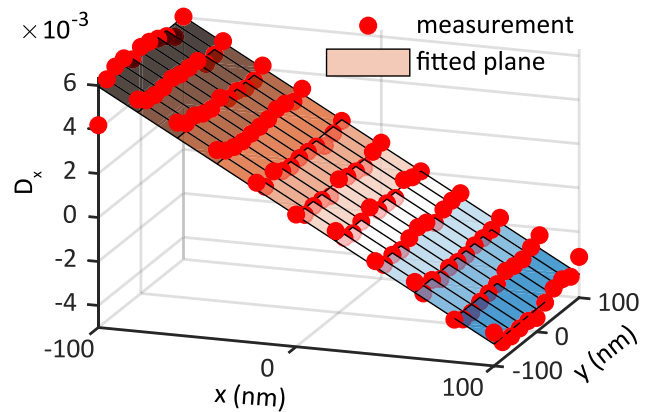


FIG. 5. Linear behavior of the sensor. Directivity D_x for a scan across an area of $200 \times 200 \text{ nm}^2$ in steps of 20 nm. Experimental data are shown as red dots, together with a planar fit $D_x(x, y)$. The linear dependence $D_x(x)$ of the measured data is quantitatively confirmed by the fit.

origin in steps of 50 nm. At each position of the five-step scan, we record 50 individual camera images with a camera integration time of 2.5 ms per image. In Fig. 6(a), the resulting directivities are shown. As expected, D_y stays almost constant, while for D_x , one can clearly distinguish the steps caused by the subsequent displacements. Here, we demonstrate the high level of accuracy of our method, as the steps of 50 nm, performed by the piezo stage, are well reflected in the measurement. For both D_x and D_y , we observe noticeable fluctuations. These mainly result from actual vibrational displacements of the sample position relative to the beam. By integrating over an area of 21×21 pixels to obtain the signal of each out-coupler, respectively, we reduce the effect of statistical fluctuations even further to a negligible level resulting from intrinsic camera noise. The overall precision is obtained by determining the standard deviation for each step and computing the mean value, leading to an average standard deviation of $\delta D_x = \pm 2.2 \cdot 10^{-4}$. The sensitivity for this measurement is $\Delta D_x = 3.0 \cdot 10^{-5}/\text{nm}$, which is a bit lower than the maximum sensitivity that was reached in the measurement corresponding to Fig. 5. The sensor resolution is then given by $\Delta x = \delta D_x / \Delta D_x = 7.2 \text{ nm}$, which is comparable to the semi-integrated position sensor demonstrated in Ref. 14. Using the respective calibration data, we reconstruct the actual position of the sample from the directivity. The x and y positions are shown in Fig. 6(b). The steps of 50 nm are well reproduced. However, the reconstructed y position also shows some slight drift behavior, which is not expected here as the piezo stage is purely moved in the x direction. The reason for this observed drift might be an actual movement in the y direction of the sample relative to the beam due to the relatively long measurement time.

In order to experimentally study the impact of fabrication imperfections leading to a non-uniform shape of the scatterer, we tested the performance of multiple other structures that were fabricated with varying dimensions and fabrication parameters. Our main observation is that an irregularly shaped scatterer leads to asymmetries in the obtained calibration maps, i.e., to directional scattering that deviates from the desired cylindrically symmetric

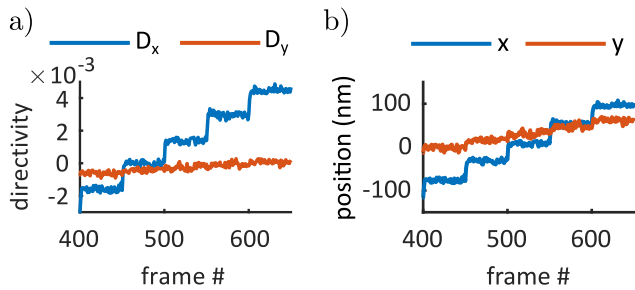


FIG. 6. Directivities (a) and reconstructed positions (b) for a line scan along the x axis with a step size of 50 nm. At each position, 50 camera images are taken. In the reconstructed position data, the steps are well reproduced.

case. Exemplary measurements for other test structures can be found in the [supplementary material](#).

VI. DISCUSSION

In summary, we designed, fabricated, and successfully tested a nanometer-precision position sensor monolithically integrated into an SOI platform. The underlying physical principle is position-dependent directional waveguide coupling, which emerges due to a combination of multiple factors. The illumination with the sculpted electromagnetic fields of a tightly focused azimuthally polarized beam leads to the excitation of electric and magnetic multipole moments in the central cylinder, exhibiting distinct emission patterns and influencing the coupling. Apart from that, also the polarization and phase of the cylinder near-fields, as well as the impedance matching to the supported waveguide modes, noticeably contribute to the observed directionality. The sensor enables position measurements with a resolution of 7.2 nm. Furthermore, the direction of the displacement can be directly inferred from the optical output, making it extremely advantageous over conventional alignment techniques, where in most cases, only information about the magnitude is provided.^{20,21} This property of our device resembles the characteristic output of a quadrant photodiode. The high-precision sensing capability is restricted to displacements in the transverse direction. To achieve sensitivity in all three dimensions, one could make use of a tailored beam that exhibits a strongly varying phase along the z direction, conceptually similar to the Gouy phase. At the same time, such a beam still needs to provide tailored electromagnetic fields in the x - y plane. Moreover, the resolution is currently limited by fabrication imperfections and the restriction of the cylinder height to 220 nm. Furthermore, the detection efficiency is comparably low due to the use of inverse tapers to couple out the light, which typically emits light in a wide angular range. Therefore, only a fraction of the light is detected by the camera. Replacing the inverse tapers with grating couplers would directly lead to an increase in detection efficiency. Alternatively, the detection of light propagating in the waveguides can be implemented on-chip as well. To that end, one could make use of integrated detectors, which, in a non-invasive manner, measure changes in electrical conductivity resulting from light propagating in the waveguides.²² The implementation of such detectors, together with a design that does not rely on a specifically tailored beam for excitation, would enable the integration of the sensor into an industrial metrology system.

Furthermore, these detectors would allow for time-resolved position sensing,¹⁹ enabling the measurement not only of position but also of velocity and acceleration. Together with an appropriate feedback loop, this would be useful for the direct compensation of environmentally induced mechanical noise in the above-mentioned systems. For such future designs, a more elaborate and flexible optimization process of the structure might be required, leading to increased sensitivity, versatility, and resolution of the sensor. To make this optimization process more efficient, inverse-design methods can be employed.²³ Apart from that, the development of a similar system working at visible frequencies would be desirable. To achieve this, one can make use of the silicon nitride platform.

SUPPLEMENTARY MATERIAL

The online version contains [supplementary material](#), including information about the multipole decomposition of the silicon nano-cylinder, the electromagnetic fields of a tightly focused linearly polarized Gaussian beam, and the influence of fabrication imperfections on the sensor behavior.

AUTHOR DECLARATIONS

Conflict of Interest

The authors have no conflicts to disclose.

Author Contributions

P.B. and P.B. conceived the idea for the integrated photonic position sensor. S.A.S. led the sample fabrication. L.C.W. carried out the patterning of the silicon structure. S.I. and L.O. applied the top cladding to the sample. P.B. carried out numerical simulations and optical measurements. P.B. supervised the project.

Paul Beck: Conceptualization (equal); Data curation (equal); Formal analysis (equal); Investigation (equal); Methodology (equal); Validation (equal); Visualization (equal); Writing – original draft (equal); Writing – review & editing (equal). **Laura C. Wynne:** Resources (supporting). **Simone Iadanza:** Resources (equal). **Liam O’Faolain:** Resources (equal). **Sebastian A. Schulz:** Methodology (supporting); Project administration (supporting); Resources (lead); Supervision (supporting); Visualization (supporting); Writing – original draft (supporting). **Peter Banzer:** Conceptualization (equal); Formal analysis (supporting); Investigation (supporting); Methodology (supporting); Project administration (lead); Resources (equal); Supervision (lead); Writing – original draft (supporting); Writing – review & editing (supporting).

DATA AVAILABILITY

The data that support the findings of this study are available from the corresponding author upon reasonable request.

REFERENCES

- ¹D. Thomson, A. Zilkie, J. E. Bowers, T. Komljenovic, G. T. Reed, L. Vivien, D. Marris-Morini, E. Cassan, L. Viot, J.-M. Fédéli *et al.*, “Roadmap on silicon photonics,” *J. Opt.* **18**, 073003 (2016).
- ²C. Doerr and L. Chen, “Silicon photonics in optical coherent systems,” *Proc. IEEE* **106**, 2291–2301 (2018).

- ³H. Subbaraman, X. Xu, A. Hosseini, X. Zhang, Y. Zhang, D. Kwong, and R. T. Chen, "Recent advances in silicon-based passive and active optical interconnects," *Opt. Express* **23**, 2487–2511 (2015).
- ⁴W. Bogaerts, D. Taillaert, B. Luyssaert, P. Dumon, J. V. Campenhout, P. Bienstman, D. V. Thourhout, R. Baets, V. Wiaux, and S. Beckx, "Basic structures for photonic integrated circuits in silicon-on-insulator," *Opt. Express* **12**, 1583–1591 (2004).
- ⁵A. Rosenthal, M. Omar, H. Estrada, S. Kellnberger, D. Razansky, and V. Ntziachristos, "Embedded ultrasound sensor in a silicon-on-insulator photonic platform," *Appl. Phys. Lett.* **104**, 021116 (2014).
- ⁶A. Annoni, E. Guglielmi, M. Carminati, G. Ferrari, M. Sampietro, D. A. Miller, A. Melloni, and F. Morichetti, "Unscrambling light—automatically undoing strong mixing between modes," *Light: Sci. Appl.* **6**, e17110 (2017).
- ⁷B. Redding, S. F. Liew, R. Sarma, and H. Cao, "Compact spectrometer based on a disordered photonic chip," *Nat. Photonics* **7**, 746–751 (2013).
- ⁸EVGroup, EVG IQ Aligner NT: Automated Mask Alignment System, https://www.evgroup.com/fileadmin/media/products/lithography/mask_alignment/iqaligner/evg_iq_aligner_nt_flyer.pdf; accessed 15 September 2022.
- ⁹S. W. Hell and J. Wichmann, "Breaking the diffraction resolution limit by stimulated emission: Stimulated-emission-depletion fluorescence microscopy," *Opt. Lett.* **19**, 780–782 (1994).
- ¹⁰E. Betzig, G. H. Patterson, R. Sougrat, O. W. Lindwasser, S. Olenych, J. S. Bonifacio, M. W. Davidson, J. Lippincott-Schwartz, and H. F. Hess, "Imaging intracellular fluorescent proteins at nanometer resolution," *Science* **313**, 1642–1645 (2006).
- ¹¹R. W. Taylor, R. G. Mahmoodabadi, V. Rauschenberger, A. Giessel, A. Schambony, and V. Sandoghdar, "Interferometric scattering microscopy reveals microsecond nanoscopic protein motion on a live cell membrane," *Nat. Photonics* **13**, 480 (2019).
- ¹²M. Neugebauer, P. Woźniak, A. Bag, G. Leuchs, and P. Banzer, "Polarization-controlled directional scattering for nanoscopic position sensing," *Nat. Commun.* **7**, 11286 (2016).
- ¹³A. Bag, M. Neugebauer, P. Woźniak, G. Leuchs, and P. Banzer, "Transverse K scattering for Angstrom localization of nanoparticles," *Phys. Rev. Lett.* **121**, 193902 (2018).
- ¹⁴A. Bag, M. Neugebauer, U. Mick, S. Christiansen, S. A. Schulz, and P. Banzer, "Towards fully integrated photonic displacement sensors," *Nat. Commun.* **11**, 2915 (2020).
- ¹⁵P. Woźniak, P. Banzer, and G. Leuchs, "Selective switching of individual multipole resonances in single dielectric nanoparticles," *Laser Photonics Rev.* **9**, 231–240 (2015).
- ¹⁶H. Rubinsztein-Dunlop, A. Forbes, M. V. Berry, M. R. Dennis, D. L. Andrews, M. Mansuripur, C. Denz, C. Alpmann, P. Banzer, T. Bauer *et al.*, "Roadmap on structured light," *J. Opt.* **19**, 013001 (2016).
- ¹⁷A. Doicu and T. Wriedt, "Calculation of the T matrix in the null-field method with discrete sources," *J. Opt. Soc. Am. A* **16**, 2539 (1999).
- ¹⁸A. Doicu, T. Wriedt, and Y. Eremin, "Light Scattering by Systems of Particles," in *Springer Series in Optical Sciences*, **124** (Springer-Verlag Berlin Heidelberg, 2006), pp. 1–324.
- ¹⁹P. Beck, M. Neugebauer, and P. Banzer, "Toward high-speed nanoscopic particle tracking via time-resolved detection of directional scattering," *Laser Photonics Rev.* **14**, 2000110 (2020).
- ²⁰M. Carminati, S. Grillanda, P. Ciccarella, G. Ferrari, M. J. Strain, M. Sampietro, A. Melloni, and F. Morichetti, "Fiber-to-waveguide alignment assisted by a transparent integrated light monitor," *IEEE Photonics Technol. Lett.* **27**, 510–513 (2014).
- ²¹G. Böttger, H. Schröder, and R. Jordan, "Active or passive fiber-chip-alignment: Approaches to efficient solutions," *Proc. SPIE* **8630**, 33–49 (2013).
- ²²F. Morichetti, S. Grillanda, M. Carminati, G. Ferrari, M. Sampietro, M. J. Strain, M. Sorel, and A. Melloni, "Non-invasive on-chip light observation by contactless waveguide conductivity monitoring," *IEEE J. Sel. Top. Quantum Electron.* **20**, 292–301 (2014).
- ²³H. Chen, J. Li, Z. Shang, G. Wang, Z. Zhang, Z. Zhao, M. Zhang, J. Yin, J. Wang, K. Guo, J. Yang, and P. Yan, "Inverse-designed integrated nonlinear optical switches," *Laser Photonics Rev.* **16**, 2200254 (2022).